Volume 26
Number 31
21 August 2024
Pages 4123–4250

CrystEngComm

rsc.li/crystengcomm

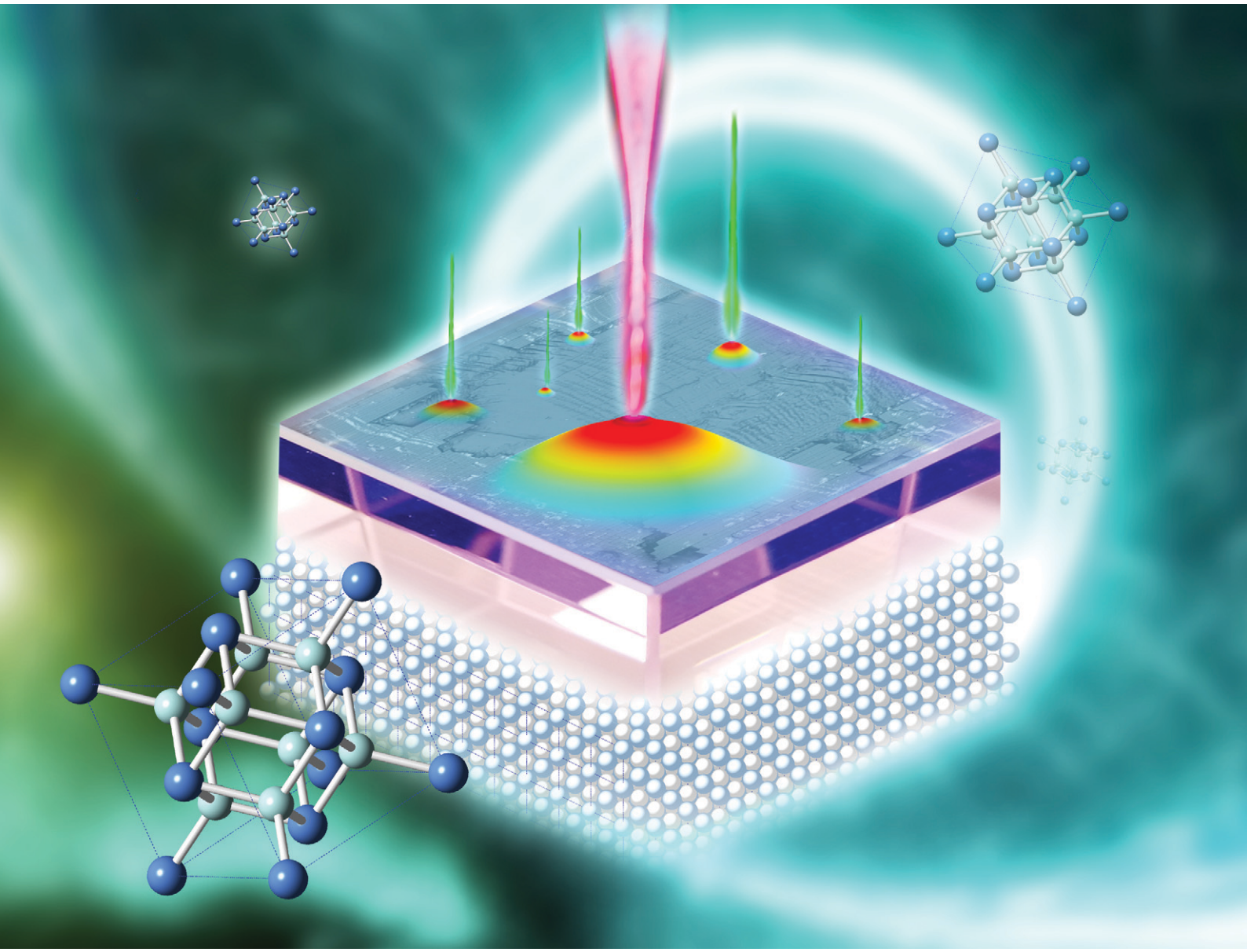

ISSN 1466-8033

ROYAL SOCIETY OF CHEMISTRY

PAPER

Anhua Wu, Liangbi Su *et al.*

Investigation of the photothermal weak absorption and laser damage characteristics of a Nd,Y:SrF_2 crystal

CrystEngComm

ROYAL SOCIETY OF CHEMISTRY

PAPER

View Article Online
View Journal | View Issue

Cite this: *CrystEngComm*, 2024, **26**, 4130

Investigation of the photothermal weak absorption and laser damage characteristics of a Nd,Y:SrF_2 crystal

Zhuowei Lu,[ab] Zhonghan Zhang,[a] Dapeng Jiang,[a] Huamin Kou,[ab] Bo Zhang,[a] Ziyuan Xu,[c] Yuanan Zhao,[c] Anhua Wu *[ab] and Liangbi Su *[ab]

Received 8th April 2024,
Accepted 1st July 2024

DOI: 10.1039/d4ce00340c

rsc.li/crystengcomm

Nd,Y:SrF_2 crystal is considered a promising laser gain material in high-energy laser systems owing to its advantages of long emission lifetime, low nonlinear refractive index and high thermal conductivity. In this study, photothermal weak absorption and laser-induced damage at 1064 nm on the surface of NYSF crystals were characterized. Based on 3D damage morphologies of cracking and bending, thermoelastic effects were considered as the damage mechanism. By analyzing weak absorption values and laser-induced damage thresholds, the exponential-Chapman quantitative relationship between laser fluence and weak absorption was observed. Additionally, the relationship between the laser fluence and growth behavior of the damaged area was investigated, indicating that the damaged area grew exponentially with an increase in fluence, and the area damaged by a secondary laser pulse was one order of magnitude larger than the primary damaged area.

1 Introduction

Significant progress has been achieved in the development of high-energy laser facilities in recent years, efficiently promoting the application of high-power laser technologies in industry, defence, high-energy physics, *etc.* For instance, following the breakthrough of a 1.3 megajoule output energy experiment in 2021,[1,2] a net energy gain was realized by the National Ignition Facility (NIF) in the United States in 2022, which is considered a milestone in the development of inertial confinement fusion (ICF) energy.[3] Nevertheless, it is still an urgent task to improve the pulse energy and repetition rate of high-power laser systems simultaneously for practical applications, and therefore, it is necessary to develop laser gain devices with the combined advantages of high thermal conductivity, large spectral bandwidth and relatively large emission cross-section. The synthesis and laser performances of novel laser gain materials such as Yb:YAG,[4,5] Yb:S-FAP (ref. 6) and Yb:CaF_2 (ref. 7–9) crystals have been reported in the past years.

Despite the fact that the fruitful efforts in increasing laser pulse energy focus on Yb^{3+}-doped materials whose energy level configuration is more suitable for the laser diode (LD) scheme,[10] the development of Nd^{3+}-doped gain materials has frequently been proposed recently because a saturation fluence of around 5 J cm^{-2} is easier to achieve in the latter category.[11,12] This saturation fluence is within the typical range of Nd^{3+}-doped phosphate glasses,[13,14] *i.e.*, the most important gain medium for high-energy laser facilities,[12,15] and is considered beneficial for generating energy pulses with high energies without increasing the risk of damaging laser gain materials. In this case, Nd^{3+}-doped laser gain materials with a moderate saturation fluence and high thermal conductivity, *e.g.*, Nd:LuAG,[16] Nd:CaF_2 (ref. 17 and 18) and Nd,Y:SrF_2,[19,20] have been developed to overcome the limitation of the low repetition rate of phosphate glasses. In 2017, a chirped pulse amplification (CPA) laser system based on Nd,Y:SrF_2 (NYSF) crystals was reported and a compressed pulse laser of 3.7 mJ energy and 1.6 ps duration at a repetition rate of 5 Hz was demonstrated.[21] In 2024, a nanosecond NYSF regenerative amplifier generating an output of 9.78 mJ energy and 1.1 MW peak power at a repetition rate of 10 Hz was reported.[22] Thus, both spectroscopic parameters and laser performances of NYSF crystals indicate their potential application in high-energy laser techniques.

Alternatively, laser gain devices continuously absorb pump light and emit laser pulses that have extremely high power density and strong electromagnetic field during their operation,[15] and therefore, high laser damage resistance is one of the basic requirements for novel gain materials such

[a] *State Key Laboratory of High Performance Ceramics and Superfine Microstructure, Shanghai Institute of Ceramics, Chinese Academy of Sciences, Shanghai 201899, China*
[b] *Center of Materials Science and Optoelectronics Engineering, University of Chinese Academy of Sciences, Beijing 100049, China*
[c] *Laboratory of Thin Film Optics, Shanghai Institute of Optics and Fine Mechanics, Chinese Academy of Sciences, Shanghai 201800, China*

as NYSF crystals with a higher pulse energy and repetition rate when applied in laser facilities. Indeed, numerous studies on laser damage phenomena have been reported, focusing on several important optical components in high-energy laser techniques such as KDP crystals,[23–25] Nd^{3+}-doped phosphate glasses[26,27] and fused silica.[28,29] The proposed laser damage mechanisms based on these studies are important for enhancing the laser damage threshold of optical components, which can be achieved by minimizing the defects that contribute to laser damage during their synthesis and processing.[30,31] Additionally, given that the laser damage phenomena vary significantly for different types of materials, a systemic investigation of laser-induced damage characteristic is crucial for the further development of novel laser gain materials such as NYSF crystals.

Herein, the laser-induced damage threshold (LIDT) of an assembly of NYSF crystals was obtained by surface damage measurement under a 1064 nm nanosecond pulse laser. Several types of defects were characterized and their relationship with the LIDT was evaluated. The dependence of the LIDT values on the photothermal weak absorption and the laser damage morphology were observed and the origin of this relationship and laser damage was discussed, respectively. Besides, the laser damage growth characteristics were discussed.

2 Experimental details

2.1 Sample preparation and roughness measurement

Nd,Y:SrF_2 crystals were grown *via* the vertical Bridgman method. High-purity raw materials (99.99%) of NdF_3, YF_3 and SrF_2 were mixed stoichiometrically. The nominal concentrations of Nd^{3+} and Y^{3+} dopants in the raw materials were 0.5 at% and 5 at%, respectively. Meanwhile, PbF_2 was added as an oxygen scavenger. The mixture was filled in a graphite crucible and loaded in a furnace chamber, which was then pumped to a vacuum of 10^{-3} Pa using a Turbe vacuum pump. The crucible was heated until the raw materials melted and the crystal growth was processed by descending the crucible throughout the temperature gradient zone of the Bridgman furnace. The crystal was cooled to room temperature at a rate of 10–20 °C h^{-1} after the crystal growth process was finished.

A series of samples with dimensions of 30 mm × 30 mm × 3 mm, labelled as NYSF-1 to NYSF-5 in the following paragraphs, was fabricated and their 30 mm × 30 mm square facets were mechanically fine polished for laser damage characterization. The 30 × 30 mm^2 side facets were also roughly polished for observation during the measurement. The average roughness (R_a) of the fine-polished facets was measured using an optical profiler (New View 8050, USA) and five points with the area of 0.5 mm × 0.5 mm were selected for the R_a characterization.

2.2 Photothermal weak absorption characterization

The general principle of the photothermal weak absorption characterization is to measure the divergence of the probe light beam due to the thermal lens effect in the fractional area where an increase in temperature occurs after the pump light beam is absorbed by certain types of defects.[32–34] The photothermal weak absorption of the NYSF samples was measured to evaluate the distribution of defects that cause local absorption. The pump light source was a CW Nd:YAG laser operating at 1064 nm with a spot diameter of 60 μm. The detection light was an He–Ne laser with an output wavelength of 632 nm and spot diameter of 1 mm, ensuring the coverage of the pump light spot. The weak absorption was tested on the surface chosen twelve points randomly.

2.3 Laser damage testing

The surface laser damage characteristics were measured on the 30 × 30 mm^2 incident surface of a series of NYSF samples. The laser damage experiment was performed using a TEM_{00} mode, Q-switched Nd:YAG laser operating at 1064 nm with a repetition rate of up to 10 Hz and a pulse duration of 11.4 ns. The nanosecond pump laser propagated through the samples with an incident angle of 23°, and the effective laser spot area was 0.75 mm^2 near the incident surface. The LIDT was tested using R-on-1 mode with a starting fluence of 1 J cm^{-2} and an energy step of 2 J cm^{-2}. A CCD camera was used to observe and determine whether the radiation sites were damaged online. Additionally, the damage growth could be measured from photographs recorded by CCD. By analysing the distribution of damaged sites under various fluences, it was possible to determine the laser damage probability and LIDT, which included the 0%, 50%, and 100% damage possibility.

3 Defects, laser damage characterization and analysis

The surface roughness maps of each NYSF sample are shown in Fig. 1 and the surface roughness values are summarized in Table 1. The roughness of all five samples was less than 1 nm, indicating that their surface was relatively flat. The roughness map of NYSF-1 showed a polish trace, which led

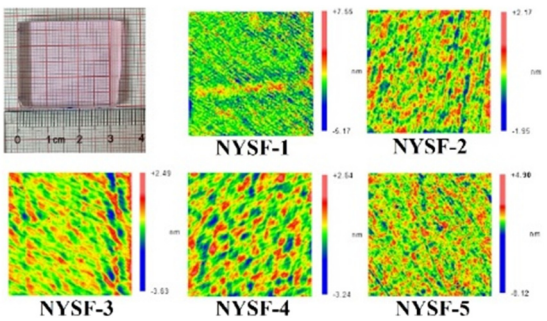

Fig. 1 Surface roughness maps of NYSF samples.

Table 1 Average surface roughness of Nd,Y:SrF_2 samples

Sample	Average surface roughness	
	R_a (nm)	RMS (nm)
NYSF-1	0.823	1.082
NYSF-2	0.325	0.412
NYSF-3	0.379	0.506
NYSF-4	0.485	0.615
NYSF-5	0.516	0.665

to obviously higher R_a and RMS roughness values. Despite this, the roughness was within the nanometre level and the influence of polishing quality on the laser damage characterization should be weak.

Photothermal weak absorption measurements were performed at the incident surfaces of all the NYSF samples. The minimum, median and maximum weak absorption values are shown in Fig. 2. Among the 5 samples, NYSF-1 had the lowest weak absorption values, and all the test points in this sample were below 10 ppm. The weak absorption of NYSF-2 to NYSF-5 increased obviously. Alternatively, the median and maximum weak absorption values of NYSF-5 were almost twice that of NYSF-3 and NYSF-4, and all the detected points in this sample showed quite high absorption.

The measured laser damage probability of the NYSF samples by the R-on-1 damage test at various laser fluences is shown in Fig. 3(a). It can be clearly seen that the NYSF-1 sample had higher laser damage resistance; meanwhile, the NYSF-5 sample was obviously easier to be damaged. The damage possibilities of the NYSF-2, NYSF-3 and NYSF-4 samples, which were manufactured under similar conditions, exhibited approximately the same trend as the increase in fluence.

The laser fluences corresponding to 0%, 50% and 100% damage probability for each sample are shown and labelled in Fig. 3(b). The LIDT is defined as the highest laser fluence incident upon the optical component for which the extrapolated probability of damage is zero,[35] corresponding

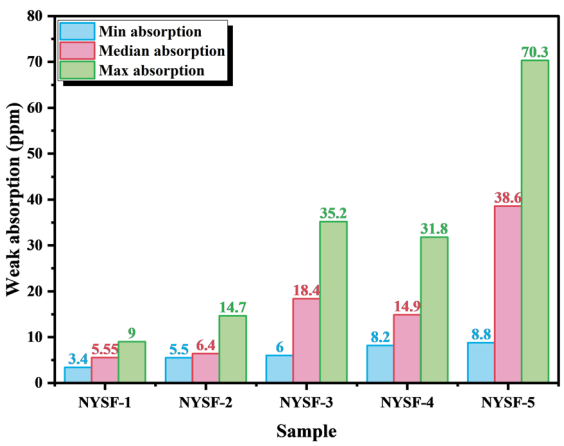

Fig. 2 Weak absorption minimum, median and maximum values of NYSF samples on the surface.

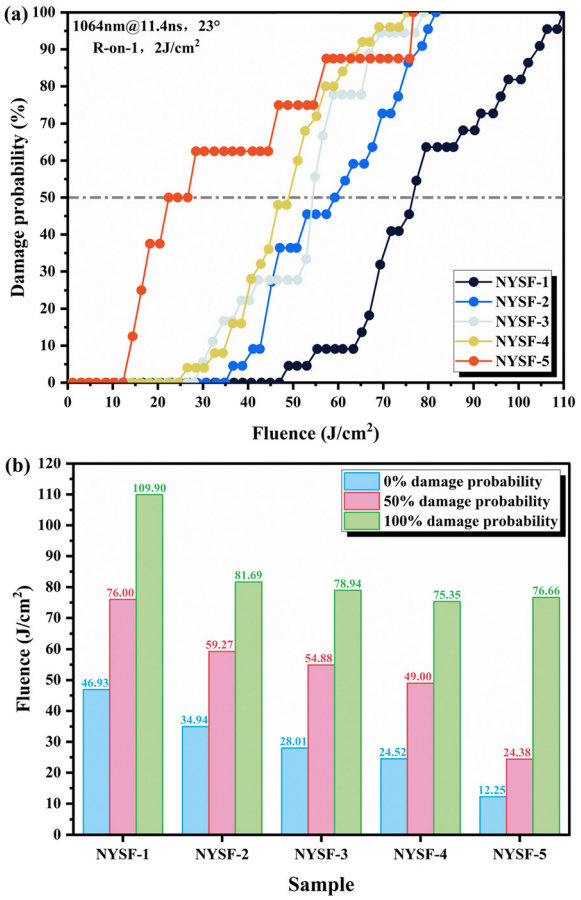

Fig. 3 (a) Laser damage probability and (b) fluence of 0%, 50% and 100% damage probability of NYSF samples.

to the 0% damage threshold in Fig. 3(b). The LIDT values of the NYSF-1 sample were the highest, reaching 46.93 J cm^{-2}; meanwhile, the LIDT of NYSF-2 slightly decreased to 34.94 J cm^{-2}. The NYSF-3 and NYSF-4 samples exhibited similar LIDT values of 28.01 and 24.52 J cm^{-2}, respectively. The LIDT of the NYSF-5 sample was only 12.25 J cm^{-2}, which is less than the half that of the NYSF-4 sample. The trends in laser fluences for 50% damage probability and 100% damage probability for these samples are generally similar to the trends of the LIDT values.

4 Discussion

4.1 Morphology of laser damage sites

As shown in the previous section, we characterized the defects associated with surface damage including roughness and photothermal weak absorption in the samples. The defects on the surface induced by the fabrication and polishing processes may be the origin of the increase in temperature in the centre part of the damage site, as shown in Fig. 4. However, according to the roughness characterization shown in Table 1, the polishing quality of most of the samples meets the requirement of laser applications. Among them, the NYSF-1 samples had the worst

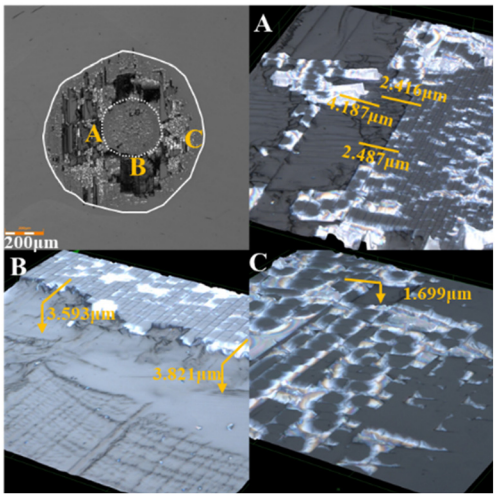

Fig. 4 Primary (dotted line) and secondary (solid line) laser damage morphologies under 46.93 J cm^{-2} and 49.00 J cm^{-2}, respectively (A and B close to the primary damage boundary and C close to the secondary damage boundary).

surface flatness, whereas they exhibited the highest LIDT values. Thus, the defects induced during polishing should not be the primary origin of the laser damage.

The dramatic variation in the LIDT values in these NYSF samples indicates that the composition and distribution of the defects in these crystals are quite different. Thus, to distinguish which types of defects primarily contributed to the damage process, it was necessary to establish an outline of the laser-induced damage mechanisms by analyzing the morphology of the damage sites. Fig. 4 shows the primary and secondary laser damage morphologies observed by laser confocal microscopy under the laser fluence of 46.93 J cm^{-2} and 49.00 J cm^{-2}, respectively. Simultaneously, the heights of the surface from the base were measured. Some of the fragments in region A of Fig. 4 were still adhered to the substrate and showed a significant upward curvature of 4.187 μm from the darker base, while the surface was removed with a thickness of about 2.4 μm. Similarly, region B is the damage morphology close to the primary damage boundary, where the surface was removed with a thickness of about 3 μm. Alternatively, region C is close to the boundary of secondary damage and the damage morphology in this region was dominated by cracking, with only a small amount of the surface of approximately 1 μm in thickness being peeled off. Therefore, the laser-induced damage sites can be divided to two types of morphology, *i.e.*, a round-shape flat area with cracks located in the centre and surrounded by an irregular area consisting of fracture and bending of the fragments without indications of melting.

During the measurement, Newton's rings due to the interference of fragments were observed, indicating that these fragments had very uniform thicknesses.[36] According to the 3D morphology data obtained from laser confocal microscopy, the thickness of the fragment peeling was around 1–3 μm and deformation of the fragments led to upward bending of about 1 μm. This size in within the range of the typical thickness of elastically deformed fragments for CaF_2 crystals,[37] whose crystal structure and thermal-mechanical properties are very close to that of NYSF crystals. Additionally, it was proven that fluorite crystals turn from elastic to plastic above 600 °C.[38] Therefore, the fragments in Fig. 4 bent upwards because the temperature near the surface is closer to the plastic transformation temperature; meanwhile, in the deeper area the materials remained brittle. Therefore, the elastic fracture due to the temperature increase in the centre part is probably the origin of these fragments. The absorption defects at 1064 nm played an important role in the process, which can be evaluated by their weak absorption.

4.2 Relationship between LIDT and photothermal weak absorption

It can be clearly observed that the weak absorption values of the samples are not related to their surface roughness, whereas obvious associated with the LIDT values. Normally, it is reasonable to assume that the minimum value of photothermal weak absorption reflects the contribution of intrinsic defects in the crystals with smaller size and weaker absorption efficiency, thus resulting in the highest possible allowed laser fluence. The sample will be damaged definitely with a higher fluence because even the 'smallest' defects will cause a dramatic thermal effect. Meanwhile, the maximum value reflects the influence of defects with a much larger size and much stronger absorption, and thus the sample possibly damaged as long as the thermal effect due to the 'largest' defect is strong enough. The median value of photothermal weak absorption can reflect the overall level of the weak absorption of the sample.

Therefore, efforts were devoted to establishing the relationship among the minimum, median and maximum values of weak absorption to the laser fluences of 100%

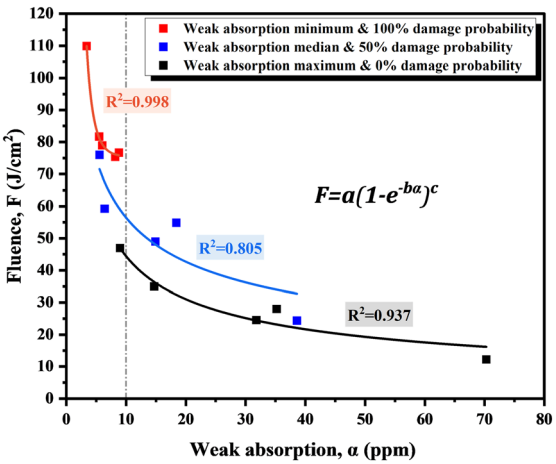

Fig. 5 Exponential-Chapman quantitative relationship between laser fluence and weak absorption.

Table 2 Exponential-Chapman function fitting parameters

Weak absorption	Laser fluence	a	b	c	R^2
Minimum	100% damage probability	75.38	0.7522	−4.675	0.9981
Median	50% damage probability	0.6626	1.619×10^{-6}	−0.4030	0.8047
Maximum	0% damage probability	0.2184	3.466×10^{-6}	−0.5175	0.9374

damage probability, 50% damage probability and 0% damage probability, respectively. As shown in Fig. 5, by using exponential-Chapman function to fit the experimental data, the relationships between the laser fluence and weak absorption were established to describe the three types of above-mentioned mechanisms. The fitting parameters are summarized in Table 2.

Additionally, as indicated in Fig. 5, the relationship between the 'maximum values of weak absorption with 100% damage probability' is more suitable to describe the influence of defects on the laser damage behaviours when the weak absorption was lower than 10 ppm. Indeed, these low absorption losses indicate that the concentration of large-size defects with strong absorption is low and the LIDT of the sample is closer to the intrinsic value of the materials. Alternatively, the relationship between the 'minimum values of weak absorption with 0% damage probability' is reliable when the weak absorption is higher than 10 ppm, where the influence of larger defects contributed decisively to the laser damage characteristics.

4.3 Surface damage growth characteristics

Besides the LIDT values, the surface damage size growth characteristics are also important to evaluate the application of optical components in high-energy laser techniques. Therefore, the damage growth was characterized by observing the laser damage morphologies of the same test point shot by a primary followed by a secondary laser pulse. Three damage growth examples at various fluences are shown in Fig. 6. The damage growth was in the form of crack expansion and flake peeling. Obviously, the size of the laser damage area was large at higher fluence and the increase in the damage area was more significant.

To describe the regular evolution of the damage sites at various fluences, the areas of all damage points shot by both primary and secondary laser pulses are shown in Fig. 7. The evolution of primary damage S_1 and secondary damage S_2 *versus* the laser fluence was fitted using $S = ae^{bF}$, where S and F are the damage area and fluence, respectively, and a and b are constants, as follows:

$$S_1 = 8692.012e^{0.311F}$$

$$S_2 = 34583.741e^{0.439F}$$

The damage area growth *versus* the laser fluence fitted well with the exponential mode. Although the weak absorption values and LIDT values of these samples varied in a large range, the damage area only increased slowly with a higher laser fluence. Meanwhile, the growth rate of the secondary damage area was greater than that of the primary damage, especially at a high fluence, where the secondary damage area was one order of magnitude lager than the primary damage area. The rapid growth in the secondary damage area is an important cause of permanent component failure.

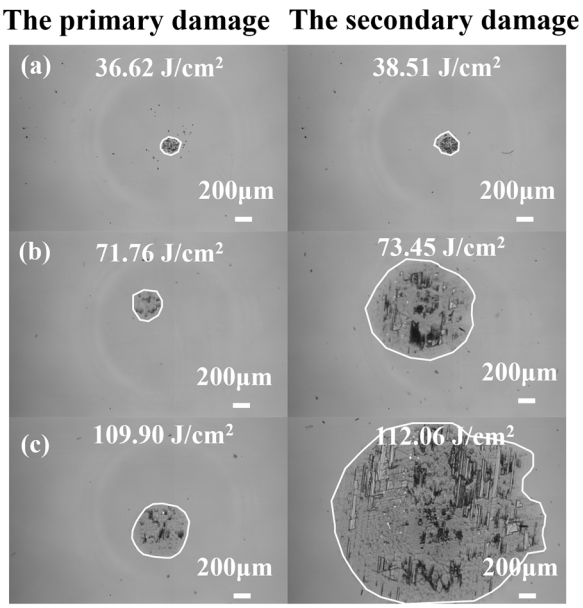

Fig. 6 Primary and secondary laser damage morphologies for the same test point at fluences of (a) 36.62 J cm^{-2}, 38.51 J cm^{-2}, (b) 71.76 J cm^{-2}, 73.45 J cm^{-2}, (c) 109.90 J cm^{-2}, 112.06 J cm^{-2}, respectively.

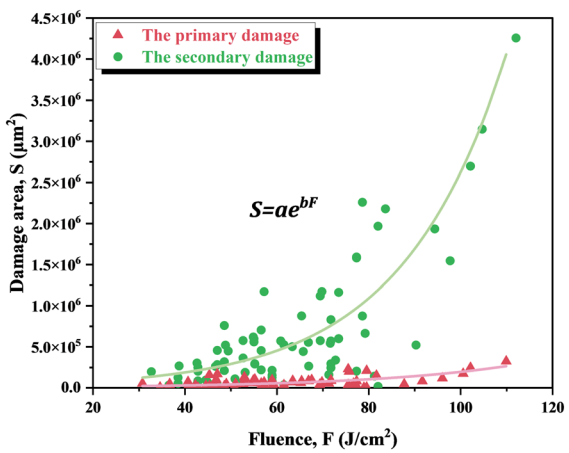

Fig. 7 Exponential relationship between the laser damaged area and fluence.

Consequently, this crystal offers a very high laser-induced damage threshold when it has very low weak absorption, but needs to be operated strictly below the damage threshold. Once damage occurs at a high fluence, the damage growth will be very significant.

5 Conclusions

In summary, we carried out a photothermal weak absorption and laser damage test using a 1064 nm laser on the surface of NYSF crystals. It was determined that the laser-induced surface damage morphologies were cracking and bending because of the thermoelastic effect by the 3D damage morphology. The absorption defects at 1064 nm were an important factor and reflected by the photothermal weak absorption. By combining the values of weak absorption with the surface and laser-induced damage characterization, the exponential-Chapman relationship between weak absorption and laser fluence was discovered. Therefore, defect-induced weak absorption is important in evaluating the laser damage performance of NYSF crystals. Additionally, it was critical that the laser damage area will grow exponentially with the laser fluence and the laser secondary damage will grow dramatically once damage occurs at a high fluence.

Data availability

Data are available on request from the authors.

Author contributions

Zhuowei Lu performed the laser damage characterization and other experiment, processed data analysis and draft writing; Zhonghan Zhang performed the optical experiment, processed data analysis and draft writing; Dapeng Jiang, Huamin Kou and Bo Zhang performed data presentation; Anhua Wu, and Liangbi Su processed data analysis and draft writing; Ziyuan Xu and Yuanan Zhao performed laser damage experiment and provided advices.

Conflicts of interest

There are no conflicts to declare.

Acknowledgements

This work has been financially supported by the National Key Technologies R&D Program (2022YFB3605702, 2021YFE0104800), the National Natural Science Foundation of China (U2230103, 61925508), the Science and Technology Commission of Shanghai Municipality (22ZR1472000), CAS Project for Young Scientists in Basic Research (YSBR-024) and State Key Laboratory of Crystal Materials, Shandong University (No. KF2202).

References

1 D. F. P. Pile, *Nat. Photonics*, 2021, **15**, 863–865.
2 Fusion news ignites optimism, *Nat. Photonics*, 2021, 15, 713.
3 D. Clery, *Science*, 2023, **378**, 6625.
4 P. Mason, D. Martin, K. Ertel, P. Jan, T. Butcher and H. Martin, *Optica*, 2017, **4**, 438–439.
5 J. Ogino, S. Tokita, S. Kitajima, H. Yoshida and J. Kawanaka, *Opt. Lett.*, 2020, **46**, 621–624.
6 A. Bayramian, J. Armstrong, G. Beer, R. Campbell, B. Chai, R. Cross, A. Erlandson, Y. Fei, B. Freitas, R. Kent, J. Menapace, W. Molander, K. Schaffers, C. Siders, S. Sutton, J. Tassano, S. Telford, C. Ebbers, J. Caird and C. Barty, *et al.*, *J. Opt. Soc. Am. B*, 2008, **25**, B57–B61.
7 M. Siebold, M. Hornung, R. Boedefeld, S. Podleska, S. Klingebiel, C. Wandt, F. Krausz, S. Karsch, R. Uecker, A. Jochmann, J. Hein and M. C. Kaluza, *Opt. Lett.*, 2008, **33**, 2770–2772.
8 A. Kessler, M. Hornung, S. Keppler, F. Schorcht, M. Hellwing, H. Liebetrau, J. Körner, A. Sävert, M. Siebold, M. Schnepp, J. Hein and M. C. Kaluza, *Opt. Lett.*, 2014, **39**, 1333–1336.
9 I. Tamer, S. Keppler, J. Korner, M. Hornung, M. Hellwing, F. Schorcht, J. Hein and M. C. Kaluza, *High Power Laser Sci. Eng.*, 2019, **7**, e42.
10 M. Siebold, J. Hein, M. Hornung, S. Podleska, M. C. Kaluza, S. Bock and R. Sauerbrey, *Appl. Phys. B: Lasers Opt.*, 2008, **90**, 431–437.
11 D. Albach, Amplified Spontaneous Emission and Thermal Management on a High Average-Power Diode-Pumped Solid-State Laser – The Lucia Laser System, *PhD Thesis*, Ecole Polytechnique ParisTech, 2010, p. 217.
12 E. Sistrunk, D. Alessi, A. Bayramian, K. Chesnut, A. Erlandson, T. Galvin, D. Gibson, H. Nguyen, B. Reagan, K. Schaffers, C. Siders, T. Spinka and C. Haefner, *Proc. SPIE*, 2019, **11034**, 1103407.
13 S. Gao, X. Xie, J. Tang, C. Fan, X. Fu, Z. Chen and K. Yao, *Frontiers in Physics*, 2022, **10**, 923402.
14 A. C. Erlandson, S. M. Aceves, A. J. Bayramian, A. L. Bullington, R. J. Beach, C. D. Boley, J. A. Caird, R. J. Deri, A. M. Dunne, D. L. Flowers, M. A. Henesian, K. R. Manes, E. I. Moses, S. I. Rana, K. I. Schaffers, M. L. Spaeth, C. J. Stolz and S. J. Telford, *Opt. Mater. Express*, 2011, **1**, 1341–1352.
15 L. Hu, D. He, H. Chen, X. Wang, T. Meng, L. Wen, J. Hu, Y. Xu, S. Li, Y. Chen, W. Chen, S. Chen, J. Tang and B. Wang, *Opt. Mater.*, 2017, **63**, 213–220.
16 T. Liu, T. Feng, Z. Sui, Q. Liu, M. Gong, L. Zhang, B. Jiang and X. Fu, *Opt. Express*, 2019, **27**, 15595–15603.
17 D. Jiang, Y. Zhan, Q. Zhang, F. Ma, L. Su, F. Tang, X. Qian and J. Xu, *CrystEngComm*, 2015, **17**, 7398–7405.
18 S. Normani, A. Braud, R. Soulard, J. L. Doualan, A. Benayad, V. Menard, G. Brasse, R. Moncorgé, J. P. Goossens and P. Camy, *CrystEngComm*, 2016, **18**, 9016–9025.
19 J. Zhu, L. Wei, W. Tian, J. Liu, Z. Wang, L. Su, J. Xu and Z. Wei, *Laser Phys. Lett.*, 2016, **13**, 055804.
20 V. Kubeček, M. Jelínek, M. Čech, D. Vyhlídal, L. Su, D. Jiang, F. Ma, X. Qian, J. Wang and J. Xu, *Opt. Quantum Electron.*, 2016, **48**, 264.

21 J. Chen, Y. Peng, Z. Zhang, H. Su, Y. Leng, D. Jiang, F. Ma, X. Qian, F. Tang and L. Su, *Opt. Commun.*, 2017, **382**, 201–204.
22 J. Guo, J. Wang, X. Lu, Y. Zhang, X. Wang, Z. Zhang, D. Jiang, L. Su, W. Fan and X. Li, *Opt. Commun.*, 2024, **557**, 130298.
23 H. Yoshida, T. Jitsuno, H. Fujita, M. Nakatsuka, M. Yoshimura, T. Sasaki and K. Yoshida, *Appl. Phys. B: Lasers Opt.*, 2000, **70**, 195–201.
24 C. Zhu, Y. Li, H. Yuan, L. Liang, J. Hao and Z. Dan, *Opt. Express*, 2022, **30**, 1327–1336.
25 S. Wang, J. Wang, X. Lei, Z. Liu, J. Zhang and Q. Xu, *Opt. Express*, 2019, **27**, 15142–15158.
26 W. Zhang and J. Zhu, *Optik*, 2008, **119**, 738–741.
27 S. Chen, Y. Chen, J. Cheng, Q. Zhou, W. Chen, L. Hu and G. Boulon, *Opt. Mater.: X*, 2019, **2**, 100032.
28 A. A. Said, T. Xia, A. Dogariu, D. J. Hagan, M. J. Soileau, E. W. Van Stryland and M. Mohebi, *Appl. Opt.*, 1995, **34**, 3374–3376.
29 Y. Li, Z. Yuan, J. Wang and Q. Xu, *Opt. Laser Technol.*, 2017, **91**, 149–158.
30 Z. Hu, P. Li, Y. Sun, J. Li and G. Zheng, *CrystEngComm*, 2022, **24**, 8440–8448.
31 Y. Li, G. Lei, X. Li, S. Sun, X. Zhao, L. Zhang, M. Xu, B. Liu and X. Sun, *CrystEngComm*, 2024, **26**, 286–292.
32 E. Welsch and D. Ristau, *Appl. Opt.*, 2005, **34**, 7239–7253.
33 J. Neauport, L. Lamaignere, H. Bercegol, F. Pilon and J.-C. Birolleau, *Opt. Express*, 2005, **13**, 10163–10171.
34 J. Liu, J. Wang and Y. Chen, *CrystEngComm*, 2022, **24**, 4983–4990.
35 ISO 21254-1:2011: Lasers and laser-related equipment – Test methods for laser-induced damage threshold – Part 1: Definitions and general principles, International Organization for Standardization, Geneva, Switzerland (2011).
36 J. Shao, X. Liang, L. You, N. Pan, Y. Lin, S. Wang, Z. Deng, X. Fang and X. Wang, *Chin. Opt. Lett.*, 2020, **18**, 021403.
37 N. Ohnishi, S. Yoshida and Y. Namba, *Mater. Trans.*, 2006, **47**, 267–270.
38 N. P. Skvortsova, E. A. Krivandina and D. N. Karimov, *Phys. Solid State*, 2008, **50**, 665–669.

